PAPER

Check for updates

A multimodal strategy of Fe₃O₄@ZIF-8/GOx@MnO₂ hybrid nanozyme *via* TME modulation for tumor therapy†

Yu Zhang,[a] Yifeng Yang,[b] Jinsheng Shi [iD] [a] and Lili Wang [iD] *[c]

Weak acidity (6.5–6.9) and limited H_2O_2 level in the tumor microenvironment (TME) usually impact the therapeutic effect of chemodynamic therapy (CDT) for cancer. A Specific TME promotes the formation of an immunosuppressive microenvironment and results in high rate of recurrence and metastasis of cancer. Fe_3O_4@ZIF-8/GOx@MnO_2 multi-layer core shell nanostructure was constructed as a hybrid nanozyme. After magnetic targeting of the tumor site, the outermost MnO_2 shell catalyzed H_2O_2 in TME to produce O_2 and was broken due to the reaction with glutathione. Due to the acid response, the ZIF-8 layer would crack and release glucose oxidase (GOx) and Fe_3O_4. The generated O_2 was utilized by GOx in starvation therapy to consume glucose and produce H_2O_2 and gluconic acid. The Fenton reaction efficiency of Fe(II) was improved by the increased H_2O_2 concentration and the enhanced acidity in TME. At the same time, the intrinsic photothermal effect of Fe_3O_4 upon 808 nm laser irradiation promoted the activity of MnO_2 and GOx as oxidase, and Fe(II) as catalase-like, and ablated the primary tumor. Moreover, the hybrid nanozyme can facilitate the transformation of M2-type macrophages to M1-type, and strong systemic antitumor immune effect was induced. A synergy of multiple therapeutic modes including starvation therapy, CDT, photothermal therapy (PTT), and immunotherapy can be realized in the hybrid nanozyme for tumor therapy.

Introduction

In the recent ten years, the incidence rate of cancer has risen by 3.9% annually and it has become a major threat to human health.[1–5] The effect of traditional treatment methods is relatively limited, including surgery, chemotherapy, and radiotherapy, which usually only inhibit the growth of the primary tumor.[6–10] The new-emerging chemodynamic therapy (CDT) has

been considered as a promising mode because of its high treatment efficiency, specificity, and minimal side effect. Peroxidase-like nanozyme has been used to catalyze intratumoral H_2O_2 into toxic hydroxyl ˙OH in CDT to induce tumor cell destruction. Endogenous chemical energy transformation has been utilized; therefore, CDT is oxygen-independent and no external energy input is needed. Fe_3O_4 nanoparticles have inherent photothermal conversion capability and Fe(II) can produce ˙OH through its Fenton reaction with H_2O_2. Therefore, Fe_3O_4 nanoparticles have been used as a photothermal and Fenton agent in photothermal therapy (PTT) and CDT, respectively.[11,12]

At the same time, PTT utilizes the heat energy obtained from laser irradiation to ablate the tumor and it is a non-invasive and precise treatment mode. The heat generated in PTT can increase the activity of glucose oxidase (GOx) and the production of ˙OH can also be accelerated in the PTT; thus, the therapeutic effect of CDT is enhanced. The cascade amplification effect can be expected in the combination of CDT, starvation therapy, and PTT.[13–15]

In recent years, nearly 90% of cancer-related deaths have been caused by metastasis rather than primary tumor growth.[16,17] Tumor immunotherapy has shown great prospects in suppressing metastatic cancer and immune checkpoint inhibitor has become one of the most effective methods for

[a]College of Chemistry and Pharmaceutical Sciences, Qingdao Agricultural University, China
[b]Department of Thyroid and Breast Surgery, The Qingdao Affiliate Hospital of Shandong First Medical University, China
[c]Science and Information College, Qingdao Agricultural University, China.
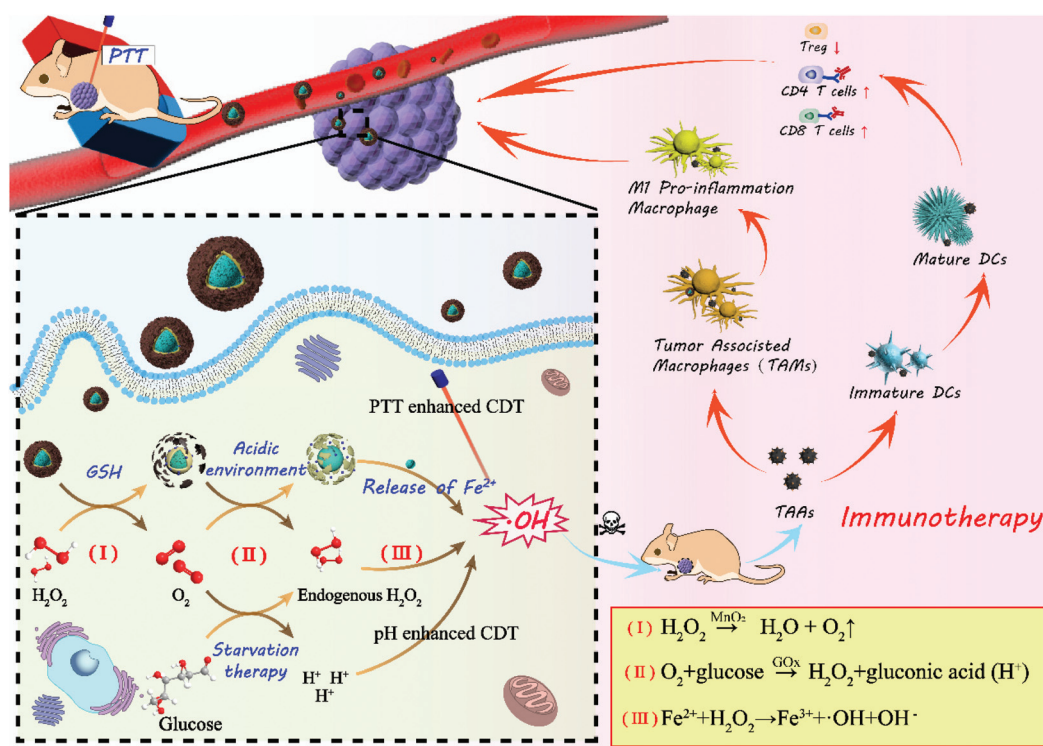E-mail: liliwang@qau.edu.cn

cancer therapy. The treatment effect of single immune checkpoint blockade is unsatisfactory because the proportion of durable responding patients is small.[18–20] It has been confirmed that phototherapy, chemotherapy, and radiotherapy can lead to primary cancer cells death and induce dying cancer cells to release tumor-associated antigens (TAAs), which can be presented to T cells receptors by dendritic cells (DCs) and then, T cell-mediated cancer immunity will be initiated.[7,18,21,22] Therefore, multimodal therapy in combination with checkpoint blockade immunotherapy (CBI) is essential to kill primary tumors and prevent metastasis. Therefore, if the CBI is accompanied with CDT, starvation therapy, and PTT, both tumor ablation *in situ* and metastasis inhibition will be achieved.

However, the reaction efficiency between Fe(II) and endogenous H_2O_2 in the tumor microenvironment (TME) is usually limited by the strict condition (low pH: 3–5).[23,24] Although the concentration of H_2O_2 in tumor cells (1.0×10^{-6} M) is much higher than that in normal cells (2.0×10^{-9} M), it is still not enough to ensure the treatment effect. In addition, the overexpression of glutathione (GSH) in TME can consume ·OH; thus, the performance of the catalytic therapy will be further affected. Starvation therapy based on GOx can provide potential solutions for this problem. Glucose can be oxidized under the catalysis of Gox; thus, the nutrition source of tumor cells will be blocked up and their proliferation can be inhibited. The generated H_2O_2 will be utilized by Fe(II), and gluconic acid provides an acidic environment for the Fenton

reaction.[25,26] Previous studies have suggested that MnO_2 can supply oxygen for starvation therapy as well as provide targeting ability because it can react with the excessive GSH in TME.

Recently, metal–organic frameworks (MOFs) have shown great potential applications in catalysis, gas storage, and drug delivery because of their large specific surface area, surface function, and enzyme carrying capacity. Therefore, GOx can be loaded in the shell after Fe_3O_4 nanoparticles are encapsulated with the zeolitic imidazolate framework-8 (ZIF-8); it can be expected that GOx will be released to oxidize glucose at the tumor site and the acidic condition will be provided for the Fenton reaction of Fe(II).[27–29]

In this paper, core–shell nanoparticles of Fe_3O_4 encapsulated by ZIF-8 were synthesized at first, as shown in Scheme 1, and then GOx was loaded in the pores of ZIF-8 by electrostatic absorption. Finally, Fe_3O_4@ZIF-8/GOx@MnO$_2$ nanoparticles (FZGM NPs) were obtained after Fe_3O_4@ZIF-8/GOx (FZG) was wrapped by MnO_2. After intravenous injection, FZGM NPs were delivered to the tumor site by the magnetic targeting of Fe_3O_4, followed by cascade catalytic reactions of MnO_2, GOx, and Fe_3O_4. MnO_2 coated in the outermost layer catalyzed H_2O_2 in the tumor cells to generate O_2 and it also can be reduced to Mn^{2+} by GSH. Then, due to the acid response ability of FZG, the ZIF-8 layer collapsed and GOx in the pores of ZIF-8 were liberated. In the presence of O_2 and GOx, glucose was oxidized into gluconic acid and H_2O_2, and the nutritional source of tumor was cut off; thus, enhanced starvation therapy was realized. Under the acidic conditions, Fe(II) played the role of a

Scheme 1 Schematic illustration of TME-responsive FZGM hybrid as a nanozyme to the trigger cascade catalytic reaction for cancer therapy.

catalase and catalyzed H_2O_2 to produce the hydroxyl radical $^\bullet OH$, which can directly kill tumor cells. Significantly, the whole process is independent of the stimulation of external energy such as laser irradiation, and it relies on TME modulation by the reasonably designed core–shell hybrid nanozyme. Under 808 nm laser irradiation, heat energy converted by Fe_3O_4 can not only ablate the tumor but also enhance the activity of MnO_2 and GOx as the oxidases, and Fe_3O_4 as the catalase, which further improved the effect of the starvation therapy and CDT. The acid response of ZIF-8 and gluconic acid produced by glucose oxidation promote the release of Fe_3O_4 and enhance the penetration ability of the $Fe_3O_4@ZIF-8/GOx@MnO_2$ (FZGM) nanozyme to the tumor cells. The cell debris produced by the combination therapy released TAAs, which were captured by DCs and presented to the T cells, inducing a specific tumor immune response. Moreover, Fe_3O_4 can also promote the transformation of M2 type macrophages to M1 type, cause inflammatory reaction, and recruit immune cells, which work together with the anti-PD-1 (α-PD-1) immune checkpoint blockade scheme to enhance the anti-tumor immune response and restrain the metastasis and recurrence of the tumor.[30]

Results and discussion

Synthesis and characterization of FZGM

Fig. 1a gives the preparation process of the FZGM hybrid nanozyme. Firstly, Fe_3O_4 was synthesized by a solvothermal reaction and the $Fe_3O_4@ZIF-8$ core–shell structure was obtained through the self-assembly of ZIF-8 on the surface of Fe_3O_4. Then, ZIF-8 was loaded with GOx by stirring and electrostatic absorption. Lastly, the outmost MnO_2 shell was directly grown on the ZIF-8 layer through sonication in aqueous $KMnO_4$ solution. The transmission electron microscopy (TEM) images of Fe_3O_4 in Fig. 1b indicate its uniformity and dispersity, and the single core–shell structure of $Fe_3O_4@ZIF-8$ can be observed in Fig. 1c. After the loading of GOx, the ZIF-8 layer no longer displays a lower contrast, which can be seen from the TEM image in Fig. 1d. The particles showed no obvious change in the mor-
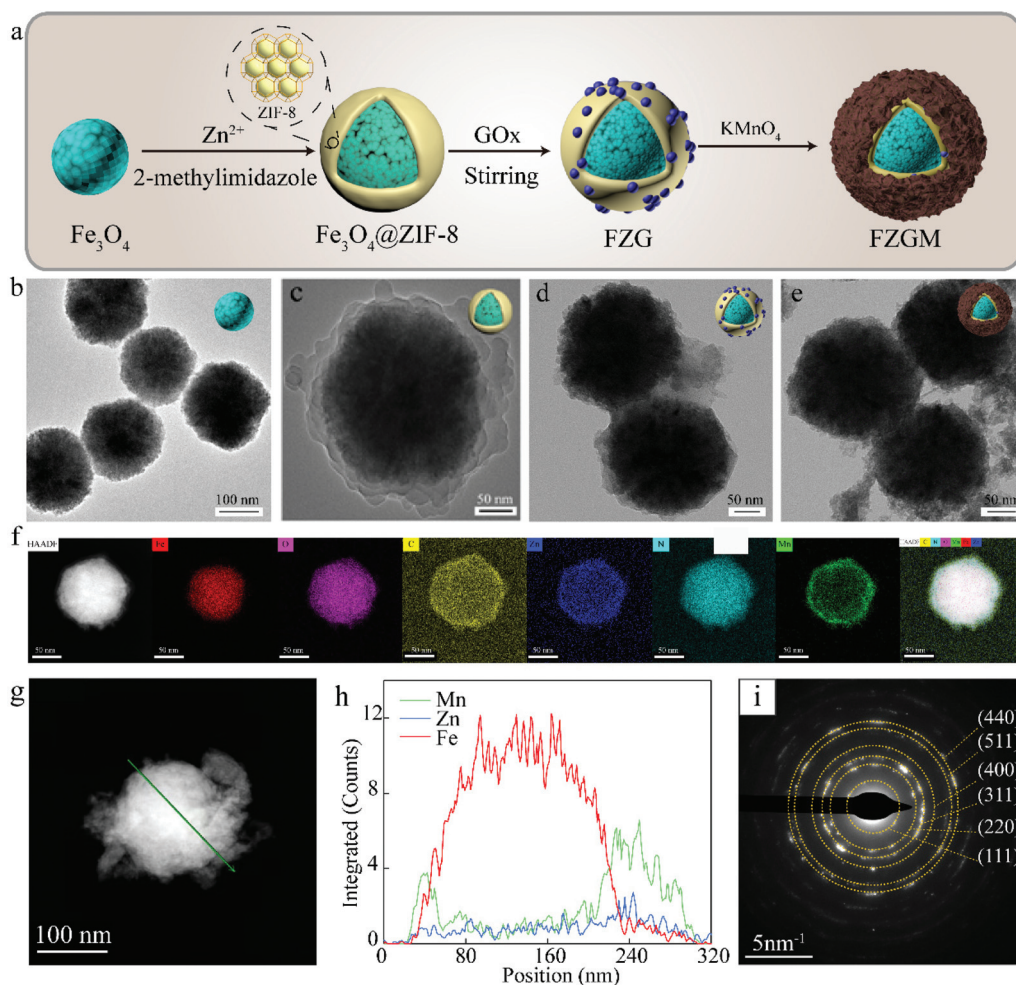

Fig. 1 (a) Schematic diagram of the fabrication process of the FZGM nanozyme. TEM images of (b) Fe_3O_4, (c) $Fe_3O_4@ZIF-8$, (d) FZG, and (e) FZGM. (f) HAADF-STEM and elemental mapping images of FZGM. (g and h) Line scan curves of FZGM. (j) SAED diffraction pattern of Fe_3O_4.

phology and diameter after the packaging of MnO_2, indicating that the MnO_2 shell is thin and easy to break when meeting H_2O_2 and GSH in TME (Fig. 1e and Fig. S1†). The as-prepared FZGM NPs was characterized by high-angle annular dark-field scanning transmission electron microscopy (HAADF-STEM) and the corresponding elemental mapping images are illustrated in Fig. 1f. It demonstrated that the Fe element is distributed in the center of the FZGM NPs, and the elemental compositions of the secondary layer are O, C, N, and Zn, which are consistent with the components of ZIF-8. Mn was found in the outmost layer and the successful coating of MnO_2 on Fe_3O_4@ZIF-8 can be confirmed. In order to further verify the formation of the three-layered nanostructure (the core of Fe_3O_4, the middle layer of ZIF-8, and the outermost shell of MnO_2), EDS line-scan of FZGM was measured and the results

are given in Fig. 1g and h. From the line profiles of Fe, Zn, and Mn, it can be clearly seen that the Fe signal is mainly in the core region and the intensity of Zn and Mn is mainly obtained in the shell. The selected area electron diffraction (SAED) pattern of Fe_3O_4 in Fig. 1i also was used to confirm the magnetic form of iron oxide and the major diffraction rings matched with the (111), (220), (311), (400), (511), and (440) planes of Fe_3O_4.

As shown in Fig. 2a, the structure of Fe_3O_4, Fe_3O_4@ZIF-8, and FZGM NPs was further verified by the X-ray diffraction (XRD) patterns. The XRD peaks of the as-prepared Fe_3O_4 NPs matched well with the standard card (JCPDS #19-0629), and they can be indexed to the cubic Fe_3O_4 phase with $Fd\bar{3}m$ space group. The characteristic peaks of ZIF-8 can be seen in the pattern of Fe_3O_4@ZIF-8, implying the successful coating of
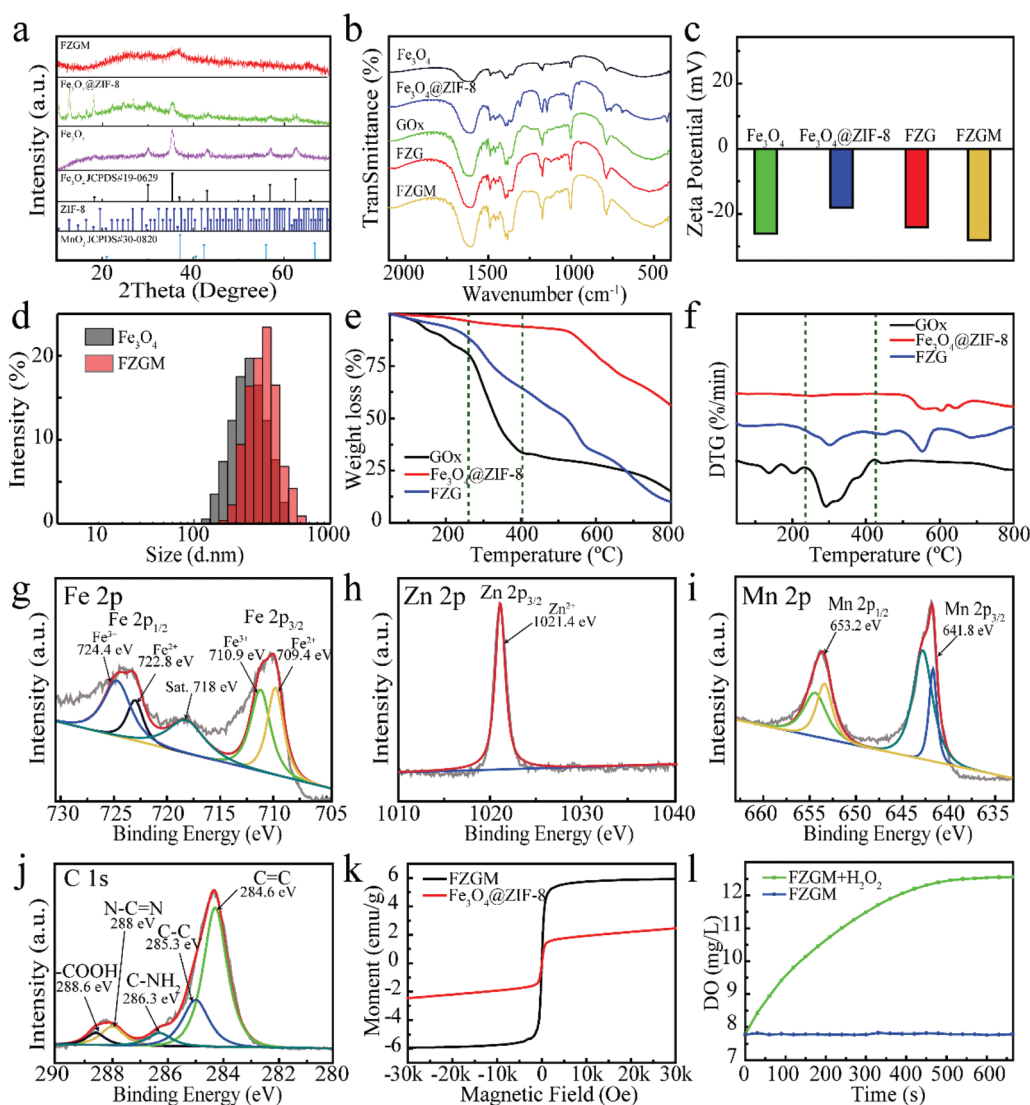

Fig. 2 (a) XRD patterns of Fe_3O_4, Fe_3O_4@ZIF-8 and FZGM. (b) FTIR spectra of Fe_3O_4, Fe_3O_4@ZIF-8, GOx, FZG and FZGM. (c) Zeta potential of Fe_3O_4, Fe_3O_4@ZIF-8, FZG and FZGM. (d) Hydrodynamic size of Fe_3O_4 and FZGM. (e) TG curves of Fe_3O_4@ZIF-8, GOx and FZG. (f) DTG curves of Fe_3O_4@ZIF-8, GOx and FZG. High-resolution XPS spectra of (g) Fe 2p, (h) Zn 1s, (i) Mn 2p and (j) C 1s in FZGM. (k) Magnetic hysteresis loop of Fe_3O_4@ZIF-8 and FZGM. (l) O_2 generation curve of FZGM aqueous solution (200 µg mL^{-1}, pH = 6.8) without and with H_2O_2 addition (100 × 10^{-6} M).

ZIF-8 layer on the Fe_3O_4 NPs. No obvious peaks with a sharp profile were observed in the XRD pattern of FZGM because of the cover of the MnO_2 shell in the outermost layer. In the Fourier transform infrared (FT-IR) spectrum of Fe_3O_4@ZIF-8, the characteristic peaks of ZIF-8 at 757 and 1146 cm^{-1} confirmed its existence (Fig. 2b). The loading of GOx in FZG and FZGM can be verified by the similar FT-IR spectra. The zeta potentials of Fe_3O_4, Fe_3O_4@ZIF-8, and FZG were measured to be −26.0, −18.1, and −24.1 mV, respectively, and that of FZGM decreased to −28.0 mV, which also indicated the successful synthesis of FZGM NPs (Fig. 2c). The average hydromechanical diameter and polydispersity index (PDI) of the FZGM NPs were 304.6 ± 88.52 nm and 0.091, respectively, as determined by dynamic light scattering (DLS). The prepared FZGM NPs were well dispersed and appeared as a brown suspension. Thermogravimetry and derivative thermogravimetry (TG-DTG) were employed to investigate the decomposition of the as-prepared samples, and the results are displayed in Fig. 2e and f. The decomposition of FZG followed a process similar to that of GOx and there are three steps in the weight loss, indicating the presence of GOx in Fe_3O_4@ZIF-8. The high weight loss for FZG occurred in the range of 260–800 °C, which was caused by the thermal degradation of both GOx and ZIF-8.[31,32] X-ray photoelectron spectroscopy (XPS) was performed to analyze the compositions and element valence state of FZGM NPs. As shown in Fig. 2g, the Fe 2p XPS spectra of Fe_3O_4 NPs gave two characteristic bands in the range of 708–713 eV and 722–726 eV, which correspond to Fe $2p_{3/2}$ and Fe $2p_{1/2}$, respectively. The lower energy band was divided into two peaks at 709.4 and 710.6 eV, and they can be assigned to Fe(II) and Fe(III), respectively. The binding energy of Fe $2p_{1/2}$ is 722.8 eV for Fe^{2+} and 724.4 eV for Fe^{3+}, respectively.[33,34] A small satellite peak at 718 eV can be observed and was originated from the oxidation of Fe_3O_4. The binding energy for Zn $2p_{3/2}$ is 1021.4 eV, as displayed in Fig. 2h.[35] The high-resolution XPS spectrum for Mn 2p consists of two bands at 641.8 and 653.2 eV, which is in agreement with Mn $2p_{3/2}$ and Mn $2p_{1/2}$, respectively, suggesting that the valence state of Mn is +4 (Fig. 2i).[36] The fine-scanned XPS of C 1s in Fig. 2j can be deconvoluted into five components centered at 284.6, 285.3, 286.3, 288, and 288.6 eV, which were attributed to C=C, C–C, C–NH_2, N–C=N, and –COOH, respectively.[37–39] The magnetic hysteresis loops of FZG and FZGM in Fig. 2k suggested that the as-synthesized NPs exhibit superparamagnetism, which will be helpful for targeting and accumulation in the tumor under an external magnetic field.[40] In order to verify the ability of MnO_2 to decompose H_2O_2 into H_2O and O_2, the dissolved O_2 in the FZGM aqueous solution (200 $\mu g\ mL^{-1}$, pH = 6.8) with or without H_2O_2 solution (100 × 10^{-6} M) was tested by a portable dissolved oxygen meter. As expected, the decomposition of H_2O_2 was triggered by FZGM and sustainable O_2 production can be observed (Fig. 2l and Fig. S3†).[41]

Photothermal performance of FZGM

In order to understand the light absorption capability of the FZGM nanozyme, the UV–Vis absorption spectra was obtained wherein FZGM exhibits strong absorption in the near UV and visible region, as shown in Fig. 3a. A thermal imager was used to study the photothermal conversion ability of Fe_3O_4 and FZGM. Under the irradiation of the 808 nm laser, the temperature increased with increasing exposure time and after 5 min, the temperature of Fe_3O_4 and FZGM was raised by 29.1 °C and 28.1 °C, respectively (Fig. 3b), indicating that the photothermal conversion ability of Fe_3O_4 was retained after the coating of ZIF-8 and MnO_2. FZGM solutions with different concentrations (0, 0.2, 0.5 mg mL^{-1}) were exposed to the 808 nm laser for 15 min and it was found that the temperature rise of FZGM is dependent on its concentration (Fig. 3c). Fig. 3d shows the photothermal response of FZGM when exposed to the 808 nm laser for 10 min; the laser was then switched off and the solution was naturally cooled to the room temperature. The linear relationship between the time value *versus* $-\ln \theta$ obtained from the cooling section of the curve in Fig. 3d is displayed in Fig. 3e. According to the reported method, the photothermal conversion efficiency η of FZGM was calculated to be 65.71%; the detailed calculation procedure is given in the ESI† (in the experimental section). In order to assess the photostability of the FZGM nanozyme, three cycles of "laser on and off" measurements were performed. As illustrated in Fig. 3f, the as-prepared FZGM showed excellent photothermal stability because there was no attenuation in its temperature rise under laser irradiation during the 3 cycles. The infrared thermal images of FZGM in Fig. 3g showed that the temperature of the FZGM solution at a concentration of 0.5 mg mL^{-1} can be raised to 61.0 °C after irradiation for 5 min, implying that it is a good photothermal agent for cancer therapy. Moreover, the raised temperature can increase the catalytic activity of GOx, which is reflected in the results of the simulation experiments in Fig. 3h. It was found that the pH value of the glucose solution containing GOx decreased with the increase in the temperature, showing that more glucose was oxidized to gluconic acid at a higher temperature (45 °C and 50 °C).

Intracellular uptake, lysosome escaping, and *in vitro* tumor penetration

Next, the cellular uptake and lysosome escaping of the FZGM nanoparticles in the 4T1 cells were visualized using a fluorescence microscope. Before the evaluation of the antitumor effect *in vivo*, the intracellular uptake of FZGM was detected by CLSM and the appearance of green fluorescence confirmed that FZGM was internalized by the 4T1 cells after 1 h incubation (Fig. 4a). Its intensity enhanced with prolonged incubation time due to the phagocytosis of the FZGM nanomaterials by the 4T1 cells. The lysosome escaping of FZGM was visualized by CLSM and the result is displayed in Fig. 4b. FZGM was captured by the lysosome at 30 min and after 1 h, the green fluorescence of FZGM separated from the red one, in which nanomaterials began to escape from the lysosome and only a very small amount of FZGM was still in the lysosome at 4 h.

The FZGM hybrid nanozyme labeled by 5-aminofluorescein (5-AF) was abbreviated as Fe_3O_4/5-AF@ZIF-8/GOx@MnO_2
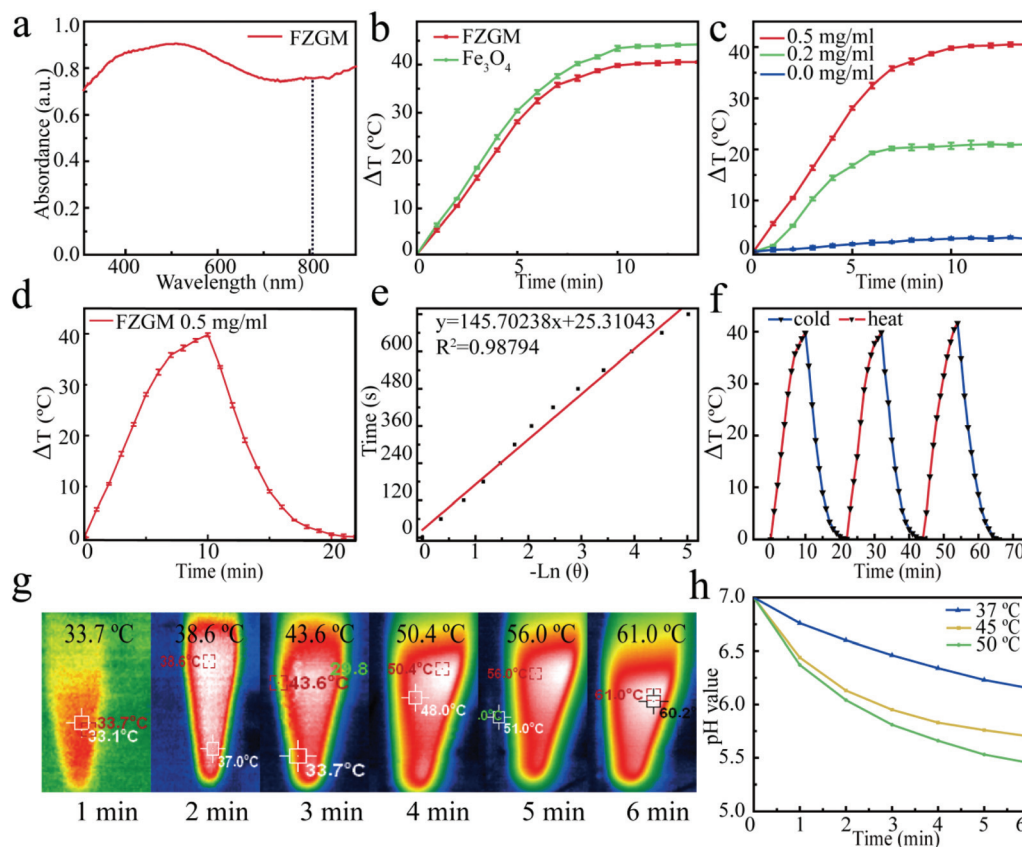
Fig. 3 (a) UV-Vis-NIR diffuse reflectance spectra of FZGM. (b) Temperature variation of Fe_3O_4 and FZGM under laser irradiation. (c) Temperature rise curves of FZGM with different concentrations under laser irradiation. (d) Temperature changes of FZGM (500 µg mL^{-1}) with laser irradiation for 10 min, and then the laser was turned off. (e) Plot of the cooling time *versus* the negative natural logarithm of the temperature driving force. (f) Temperature changes and (g) infrared thermal images of the FZGM aqueous solution (500 µg· mL^{-1}) during three on/off cycles under laser irradiation. (h) Variation in the pH values of the GOx aqueous solution at different temperatures (Laser irradiation used: 808 nm, 1.0 W cm^{-2}).

(FAZGM) and 5-AF was connected to Fe_3O_4. The *in vitro* permeability of FAZGM was evaluated by the multicellular spheroid (MCSs) model. As shown in Fig. 4c and d, the green fluorescence of 5-AF was found only in a small number of peripheral cells (groups I and III) when the 4T1 cells were incubated with Fe_3O_4/5-AF@ZIF-8@MnO_2 nanoparticles (FAZM NPs), indicating that the cell penetration ability of the FAZM NPs was inadequate. For the FAZGM nanoparticles (groups II, IV, and V), green fluorescence is widely distributed in the central area of the MCSs only in the condition of pH = 6.5 and in the presence of glucose (group IV). Therefore, the good permeability of FAZGM can be attributed to the fact that the mild acidic environment in the TME and gluconic acid generated in the oxidation of glucose work together to promote the release of Fe_3O_4 due to the acid response capability of the ZIF-8 shell, thus enhancing its tumor cell penetration ability.

In vitro cytotoxicity of FZGM

The highly efficient cellular uptake and excellent lysosomal escape capacity of the FZGM NPs encouraged us to further study the performance *in vitro*. It is known to all that GSH can counteract intracellular ROS, including ˙OH, which can confer

the resistant ability to the cancer cells. The MnO_2 shell in FZGM can deplete the GSH in the TME through its reaction with GSH (Fig. 5a) and it is very helpful for reducing the antioxidant capacity of the cancer cells and inducing cellular apoptosis. The depletion of GSH was simulated *in vitro* and the results are given in Fig. 5d. Compared with the absorbance of the GSH solution alone (8.9×10^{-5} M), when FZGM with different concentrations was added into the GSH solution, the intensity of the absorption peak decreased with increasing FZGM contents. This indicated that MnO_2 can oxidize GSH to GSSG and the cellular antioxidant system can be destroyed to a certain extent. In addition, the catalytic oxidation activity of FZGM for glucose was investigated; an illustration of the reactions is given in Fig. 5b. GOx in FZGM can catalyze glucose to produce H_2O_2 and gluconic acid, which can oxidize colorless 3,3′,5,5′-tetramethyl-benzidine (TMB) into blue-green chromogenic oxidized TMB (ox-TMB). When the FZGM nanozyme was added to the glucose solutions with different concentrations (0, 1, 2, 4, 8 mg mL^{-1}), the catalyzed oxidation of glucose brought about the generation of H_2O_2, which can be detected by the TMB-H_2O_2 colorimetric experiment. From the absorbance curves of ox-TMB in Fig. 5e, it can be seen that the
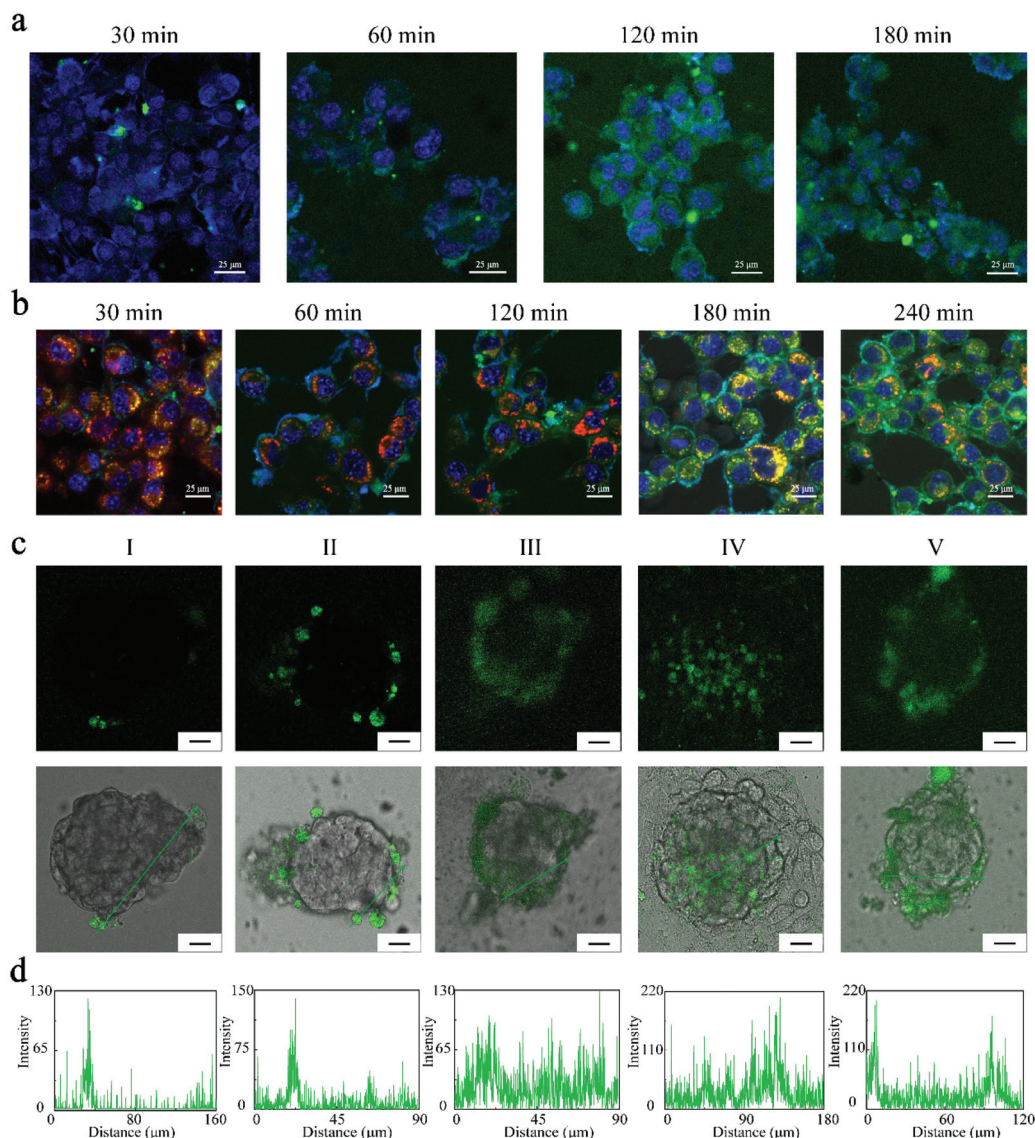
Fig. 4 (a) Intracellular uptake of FZGM NPs examined by CLSM after various incubation times. Blue fluorescence represents the nucleus and green fluorescence represents the FZGM NPs. (b) Intracellular colocalization of the 5-AF-labeled FZGM NPs with lysosomes. Green fluorescence represents FZGM NPs, and blue fluorescence represents the nucleus; red fluorescence represents lysosomes, and yellow fluorescence represents the overlay of FZGM NPs and the lysosomes in panel (b); (c) penetration of different formulations into multicellular spheroids. Scale bar: 25 μm. (d) Semi-quantitative fluorescence was performed along the line drawn on the sections in (c). (I: pH = 7.4 (+) FAZM, II: pH = 7.4 (+) FAZGM, III: pH = 6.5 (+) FAZM, IV: pH = 6.5 (+) FAZGM, V: pH = 6.5 (−) FAZGM).

amount of H_2O_2 generated increased with increasing glucose concentration, indicating that glucose can be consumed by GOx in the FZGM nanozyme. Interestingly, the effective Fenton reaction of Fe(II) can proceed with the aid of the produced H_2O_2 and gluconic acid; therefore, methylene blue (MB) served as the indicator to verify the peroxidase-like performance of FZGM NPs (Fig. 5c). As shown in Fig. 5f, when the concentration of glucose was raised from 1 to 8 mg mL^{-1}, MB degradation was enhanced by more ˙OH production, *i.e.*, the efficiency of the Fenton reaction of Fe(II) can be improved by the generated acid and H_2O_2. Through the cascade catalytic reactions, the collaboration of starvation therapy and CDT was

achieved. For further confirmation, ˙OH generation was monitored *via* electron spin resonance (ESR) using 5,5-dimethyl-1-pyrroline*N*-oxide (DMPO) as the spin trapping agent. DMPO-OH spin adducts with a quartet ESR signal formed after the reaction of DMPO with ˙OH (Fig. S4†). The generation of ˙OH in the 4T1 cells based on the Fenton reaction of Fe(II) was tested using 2,7-dichlorofluorescin diacetate (DCFH-DA) as the probe. DCFH-DA was used to stain the 4T1 cells after incubation with PBS, Fe₃O₄, FZG, FZGM, and FZGM, and only the last group was irradiated by the 808 nm laser. The confocal laser scanning microscopy (CLSM) images in Fig. 5g showed that nearly no green fluorescence of 2,7-dichlorofluorescin
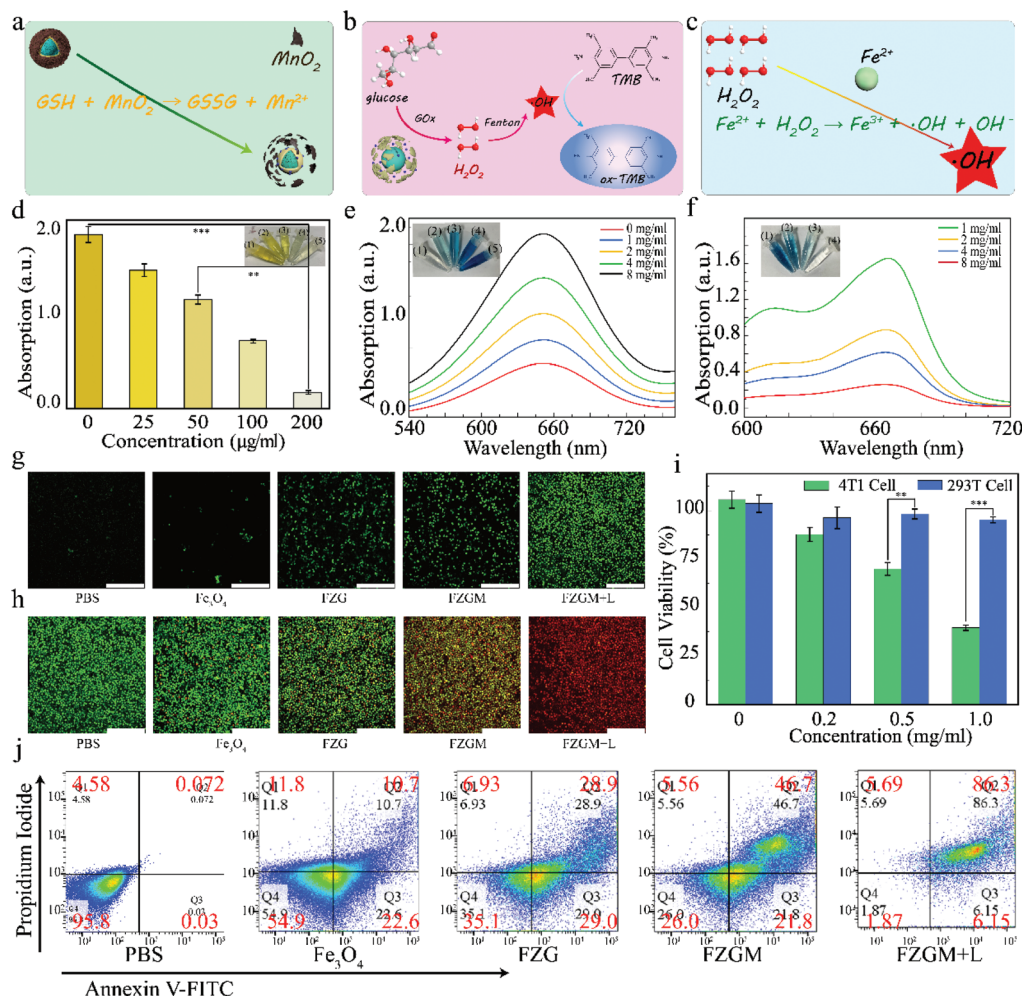
Fig. 5 (a) Illustration of the reaction between MnO_2 and GSH. (b) Schematic illustration of the generation of H_2O_2 by the oxidation of glucose. (c) Illustration of the Fenton reaction of Fe(II). (d) The ability of the FZGM nanoenzymes with different concentrations to deplete GSH: (1) 0 µg mL^{-1}, (2) 25 µg mL^{-1}, (3) 50 µg mL^{-1}, (4) 100 µg mL^{-1}, and (5) 200 µg mL^{-1}. (e) The absorbance of ox-TMB and the concentrations of the used glucose PBS solution are (1) 0 mg mL^{-1}, (2) 1 mg mL^{-1}, (3) 2 mg mL^{-1}, (4) 4 mg mL^{-1}, and (5) 8 mg mL^{-1}. (f) Degradation of MB showing the level of ·OH generated by FZGM (500 µg mL^{-1}) and glucose PBS solutions with different concentrations: (1) 1 mg mL^{-1}, (2) 2 mg mL^{-1}, (3) 4 mg mL^{-1}, and (4) 8 mg mL^{-1}. (g) Confocal fluorescence imaging of the DCFH-DA-treated 4T1 cells in different groups (I: PBS, II: Fe_3O_4, III: FZG, IV: FZGM, V: FZGM + laser). Scale bar: 250 µm. (h) Confocal fluorescence imaging of calcein AM (green) and propidium iodide (PI, red) stained 4T1 cells in different groups (I: PBS, II: Fe_3O_4, III: FZG, IV: FZGM, V: FZGM + laser). Scale bar: 250 µm. (i) 4T1 and 293T cells viability incubated with FZGM for 24 h at different concentrations. (j) Flow cytometric analysis of live and dead 4T1 cells in different treatment groups (I: PBS, II: Fe_3O_4, III: FZG, IV: FZGM, V: FZGM + laser) (Laser irradiation used: 808 nm, 1.0 W cm^{-2}). All data are presented as mean ± SD (**$p < 0.01$, ***$p < 0.001$).

(DCF) could be observed in the PBS and Fe_3O_4 groups. The weak green fluorescence in the FZG and FZGM groups indicated that slow and weak Fenton reaction occurred. Comparatively, after 808 nm laser irradiation, much brighter green fluorescence can be seen in the CLSM images of the 4T1 cells treated with FZGM, implying that more DCFH was oxidized by ·OH and the efficiency of the Fenton reaction was greatly improved by the photothermal effect of Fe_3O_4. ROS generation was also detected by flow cytometry and similar results were obtained (Fig. S5†).

The live and dead cell staining assay was utilized to evaluate the ability of the FZGM nanozyme to induce cancer cell apoptosis. As given in Fig. 5h, very intense red fluorescence can be

observed in group VI, confirming the high cytotoxic activity of FZGM on the 4T1 cells. The toxicity of the nanozyme was assessed by monitoring the cell viability of the 4T1 and 293T cells treated by FZGM with different concentrations. As shown in Fig. 5i, decreased viability can be found in 4T1 cells treated with Fe_3O_4 or FZGM, resulting from the generated ·OH in the Fenton reaction of Fe(II) with intracellular H_2O_2. Comparatively, due to the limited H_2O_2 in the 293T cells, FZGM hardly affected its viability. After the different treatments of the 4T1 cells in the six groups, flow cytometric analysis was used to detect the live and dead cells stained with FITC-Annexin V and PI, respectively. In agreement with the CLSM and CCK-8 results, laser irradiation combined with

FZGM induced more apoptosis in the 4T1 cells, and Fe_3O_4 alone without 808 nm laser exposure had little influence on the cell viability (Fig. 5j).

In vivo magnetic targeting synergistic therapy

To evaluate the treatment effect *in vivo* of the FZGM-mediated combined therapy plus α-PD-1 for the primary and distant tumors, the bilateral 4T1-tumor-bearing mice model was carefully investigated. The treatment procedure for the tumor-bearing mice is illustrated in Fig. 6a. The tumor at the right was specified as the primary tumors, and the left one was not treated and designated as the metastatic tumor. All the tumor-bearing mice were randomly divided into six groups: I: PBS, II: α-PD-1 alone, III: FZGM plus laser irradiation, IV: FZGM plus magnetic field, V: FZGM plus laser irradiation and magnetic field, VI: FZGM-α-PD-1 plus laser irradiation and magnetic

field. FZGM NPs were intravenously injected into the primary tumors of all the mice except for the PBS and α-PD-1 groups on days 1, 3, 5, 7, and 9. The α-PD-1 antibody was given to the mice in groups II and VI by intravenous injection on days 3, 5, and 7. From the infrared images of the tumor-bearing mice in Fig. S6,† it can be clearly seen that the temperature of the tumor site significantly increased after the injection of the FZGM PBS solution, followed by laser exposure, indicating that FZGM NPs have been successfully targeted at the tumor site.

The photographs of the excised tumors revealed that α-PD-1 alone shows very weak inhibition on both the primary and distant tumors (group II in Fig. 6b and in Fig. 6g). Comparatively, the treatment is effective on the initial tumor in the FZGM + laser + mag group but it has little inhibitory effect on the metastatic tumor (group V in Fig. 6b and group III in Fig. 6g). It is noteworthy that the curative effect of FZGM
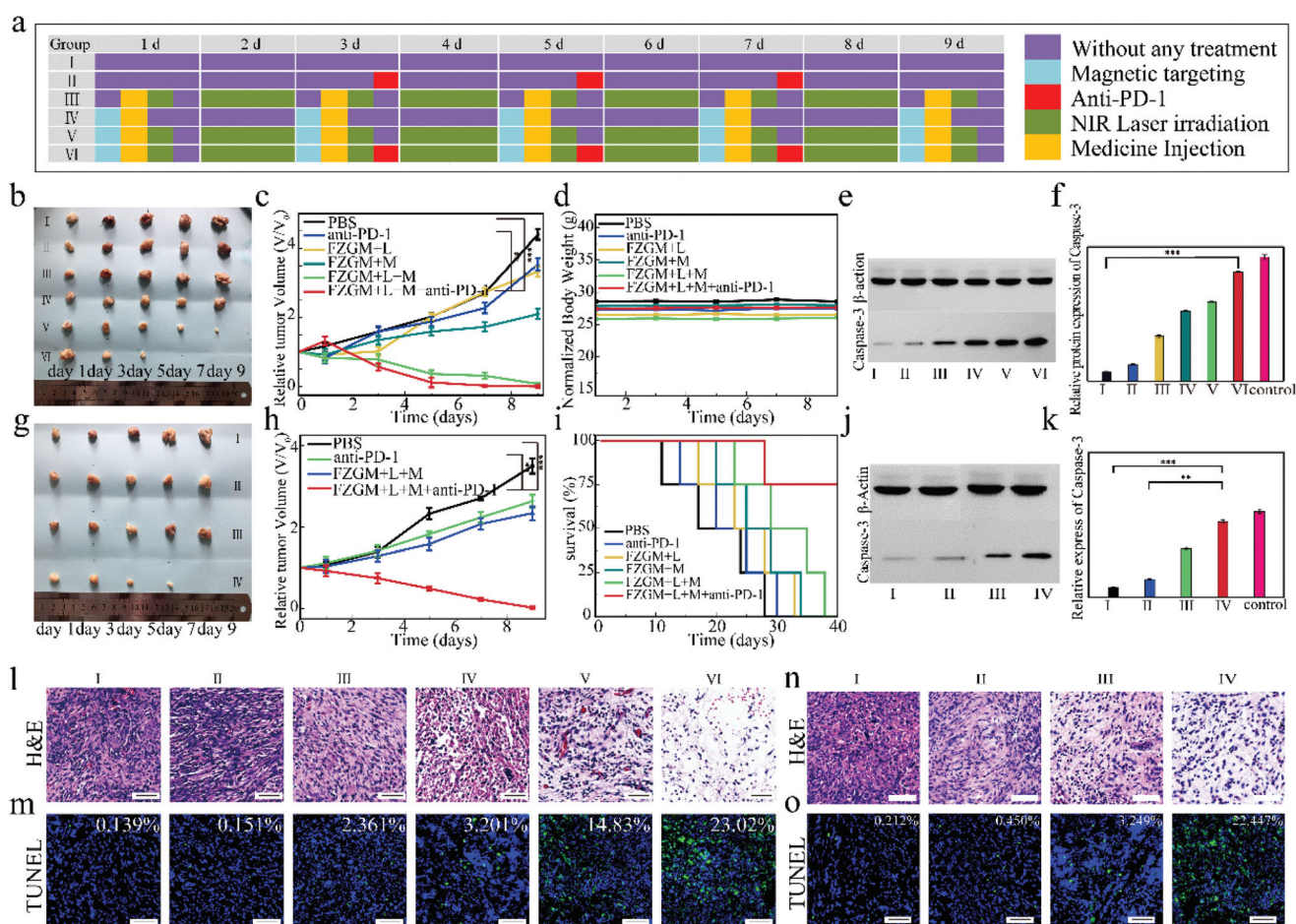

Fig. 6 (a) Schematic illustration of the experimental design for tumor treatment *in vivo*. The photos of (b) primary tumors and (g) distant tumors extracted from the mice after different treatments for 9 days. The growth curves of (c) the primary tumor volume and (h) the distant tumor volume. (d) Body weight and (i) the survival rates of the 4T1-tumor-bearing Kunming mice with different treatments. (l) H&E staining, (m) TUNEL staining of the primary tumor slices in different groups on day 9. (e) Western blotting of caspase-3 protein in the primary tumors in different groups and (f) quantitative determination. (n) H&E and (o) TUNEL staining of the distant tumor slices in different groups at the 9th day. (j) Western blotting results of the distant tumor slices in different groups and (k) quantitative determination (Treatment groups of primary tumors: I: PBS, II: α-PD-1, III: FZGM + laser, IV: FZGM + mag, V: FZGM + laser + mag, VI: FZGM-α-PD-1 + laser + mag. Treatment groups of distant tumors: I: PBS, II: α-PD-1, III: FZGM + laser + mag, IV: FZGM-α-PD-1 + laser + mag) (Laser irradiation used: 808 nm, 1.0 W cm^{-2}). All data are presented as mean $\pm$ SD (**$p < 0.01$, ***$p < 0.001$).

NPs plus α-PD-1 is the most satisfactory, and it not only eradicated the primary tumor but also nearly completely eliminated the distant one (group VI in Fig. 6c and group IV in Fig. 6h). The weight of all the mice in different treatment groups was not significantly reduced, suggesting the excellent biocompatibility of the FZGM hybrid nanozyme (Fig. 6d). The survival rate of the mice was closely monitored and it was found that 75% of the mice could survive more than 30 days after FZGM-based PTT/CDT/starvation therapy plus α-PD-1 (Fig. 6i). The mice in the other five groups all died within 38 days, indicating that the combination of the FZGM hybrid nanozyme and immune checkpoint blockade could increase the survival rate. The expression of caspase-3 was estimated from quantitative western blot analysis and the highest expression level was found in the tumor tissues of the mice treated with FZGM plus α-PD-1 in group VI (Fig. 6e and f), which implied that the combination of FZGM and α-PD-1 can significantly induce the apoptosis of the cancer cells. The greatest expression of caspase-3 in the distant tumor tissues can be observed in group IV, which also indicated that tumor cell apoptosis was induced by the immune response (Fig. 6j and k). Moreover, hematoxylin and eosin (H&E) staining and the terminal deoxynucleotidyl transferase (TdT)-mediated dUTP nick end labeling (TUNEL) assay of the tumor tissues collected after treatment further confirmed the most effective treatment effect of group VI (Fig. 6l and m). For the distant tumor, α-PD-1 alone had

Fig. 7 Representative images of the primary tumors slices stained for (a) CD4+ T cells, (b) CD8+ T cells, (c) M1 macrophages, (d) M2 macrophages, and (e) Treg cells after the different treatments. The contents of (f) TNF-α, (g) IFN-γ, (h) IL-12, (i) TGF-β, (j) IL-10, and (k) Granzyme B (I: PBS, II: α-PD-1, III: FZGM + laser, IV: FZGM + magnetic targeting (mag), V: FZGM + laser + mag, VI: FZGM-α-PD-1 + laser + mag). Scale bar is 50 μm (808 nm laser irradiation, 1.0 W cm^{-2}). All data are presented as mean ± SD (**$p < 0.01$, ***$p < 0.001$).

little treatment effect, which can be concluded from the analysis of H&E and TUNEL staining of the distant tumor tissues in Fig. 6n and o.

Mechanism of action to inhibit the growth of primary and distal tumors

In order to understand the mechanism of action of the as-prepared FZGM for destroying the tumor cells, the infiltrated lymphocytes in the primary tumor tissues were examined by immunofluorescence imaging. Compared with the control group, the intratumoral infiltration of the cytotoxic T lymphocytes (CTLs) was promoted by FZGM-mediated combined therapy. The proportion of CD4$^+$ T cells in group III, IV, and V was 2.16-fold, 2.93-fold, and 4.06-fold higher than that of the PBS group, respectively (Fig. 7a). The increase in the CD8$^+$

CTLs was also found in the three groups in Fig. 7b. In group VI, α-PD-1 antibody was used to enhance the antitumor immune effect and it can be observed that the tumor-infiltrating CD4$^+$ cells and CD8$^+$ CTLs were greatly increased to 6.18-fold and 50.0-fold, respectively, compared with the control group. The results showed that FZGM could induce immune response to kill the tumor cells, and the magnetic targeting of Fe$_3$O$_4$ as well as 808 nm laser irradiation have immunological enhancement effects. In combination with the α-PD-1 antibody, the infiltration of the lymphocytes was significantly improved. It has been reported that intratumoral hypoxia can promote the polarization of tumor-associated macrophages (TAMs) to M2 type, which is the critical factor of immunosuppressive TME. Fe$_3$O$_4$ based on the Fenton reaction can transform M2 to M1 macrophages to improve the antitumor

Fig. 8 Representative immunofluorescence images of distant tumors stained for (a) CD4$^+$ T cells and (b) CD8$^+$ T cells, (c) M1 macrophages, (d) M2 macrophages and (e) Treg cells after the different treatments. The contents of (f) TNF-α, (g) IFN-γ, (h) IL-12, (i) TGF-β, (j) IL-10 and (k) Granzyme B of distant tumors in different groups at the 9th day (I: PBS, II: α-PD-1, V: FZGM + laser + mag, VI: FZGM-α-PD-1 + laser + mag). Scale bar is 50 μm. (808 nm laser irradiation, 1.0 W cm^{-2}). All data are presented as mean ± SD (**p < 0.01, ***p < 0.001).

immune reaction.[20,40,42,43] Therefore, the influence of the FZGM-mediated combined therapy on TAMs polarization was studied and immunofluorescence assay was used to study the TAMs phenotypes, which mainly contains CD86 antitumor M1-type macrophages and CD206 protumoral M2 type macrophages. As illustrated in Fig. 7c and d, the FZGM-mediated combined therapy resulted in the up-regulation of CD86 and down-regulation of CD206. After the accumulation at the tumor site and laser irradiation, FZGM with α-PD-1 induced CD86 expression (group VI in Fig. 7c). Moreover, for group V, the CD86 expression was up-regulated more than 10 times compared with that of the control group, suggesting that macrophage polarization toward M1 type was promoted by the FZGM nanoplatform. In addition, the amount of Foxp3 regulatory T cells (Treg cells) decreased in the FZGM + laser + mag and FZGM-α-PD-1 + laser + mag groups, indicating that immunosuppression was partially relieved with or without the help of α-PD-1 immune checkpoint blockade (Fig. 7e). Finally, the secretion of tumor cytokines in the tumor was examined by enzyme-linked immunosorbent assay (ELISA), including TNF-α, IFN-γ, IL-12, IL-10, TGF-β, and granzyme B (GZMB). A high level of TNF-α, IFN-γ, and IL-12 expression occurred in the FZGM-α-PD-1 + laser + mag group, which was 4.78-fold, 4.78-fold, and 8.73-fold higher than that of the counterparts in the control group, respectively (Fig. 7f–h). The secretion of immunosuppressive cytokines was studied and the results in Fig. 7i and j reveal that FZGM-exposed macrophages down-regulated the expression of the immunosuppressive cytokines TGF-β and IL-10. As shown in Fig. 7k, the expression of GZMB in group VI is the highest and a large amount of GZMB was secreted by the cytotoxic immune cells, which is attracted by the inflammatory cytokines and chemokines, indicating that the antitumor activity in the FZGM-α-PD-1 + laser + mag group is the strongest.

From the discussion above, it can be concluded that the designed FZGM cascade hybrid nanozyme has a great killing effect on the primary tumor. However, cancer metastasis and recurrence can cause a lot of pain and a series of symptoms, thus increasing the mortality of the patients. Therefore, the inhibition of the hybrid nanozyme on the distant tumor was evaluated, and the results are given in Fig. 8. The tumor-infiltrating T lymphocyte for the distant tumor was first analyzed (Fig. 8a and b). The proportion of the CD4$^+$ and CD8$^+$ cells in the distant tumor of FZGM-α-PD-1 + laser + mag treated mice increased significantly relative to that in the FZGM + laser + mag group, demonstrating that the α-PD-1 checkpoint blockade played a major role in increasing the specific T cell infiltration in the metastatic tumor. However, compared with the
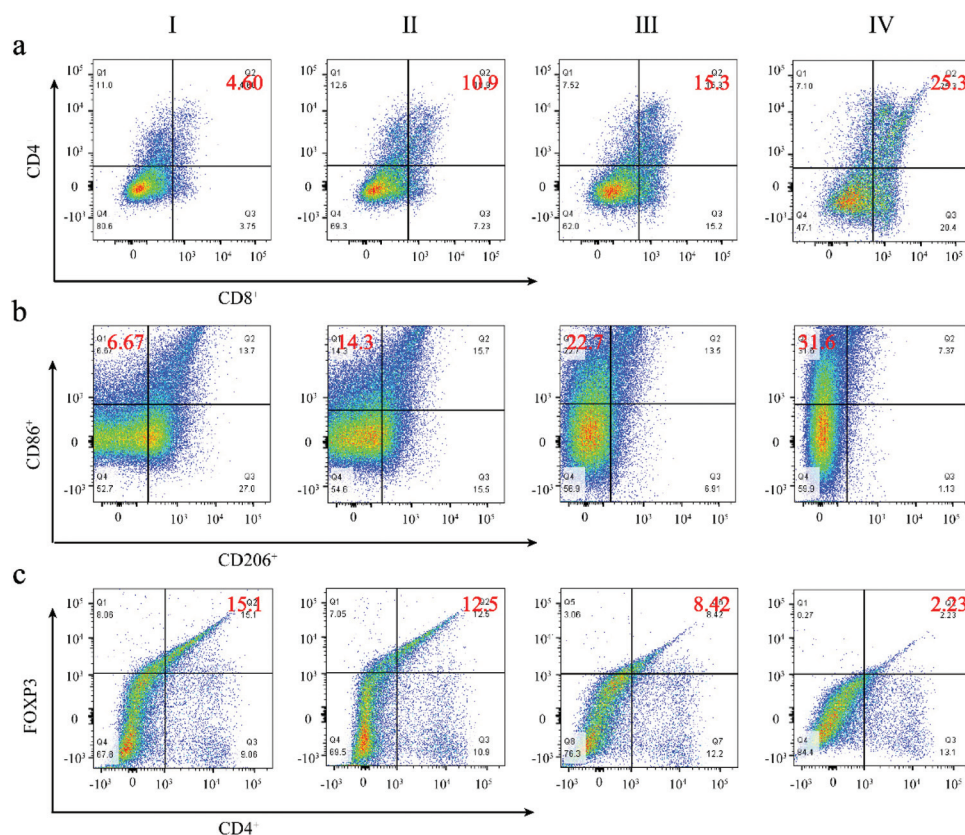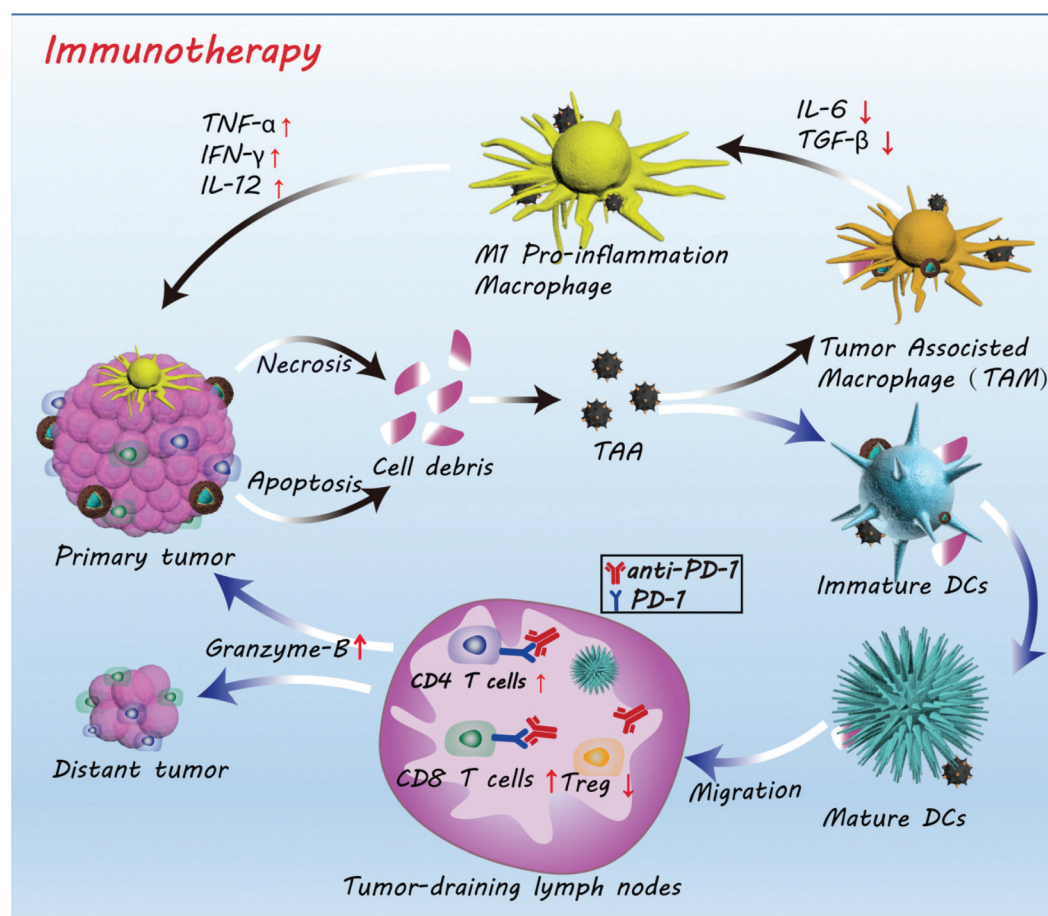

Fig. 9 Flow cytometric analysis of distant tumors stained for (a) CD4$^+$ and CD8$^+$ T cells, (b) polarization of macrophages and (c) Treg cells from 4T1 tumor-bearing mice after the different treatments (I: PBS, II: α-PD-1, III: FZGM + laser + mag, IV: FZGM-α-PD-1 + laser + mag) (808 nm laser irradiation, 1.0 W cm^{-2}).

control group, the infiltration of the T cells in the α-PD-1 group did not increase much. This shows that the α-PD-1 antibody alone cannot play a very good inhibitory effect on the metastatic tumors without the FZGM cascade nanozyme. Under the premise of TAAs released by the combined therapy, FZGM showed vaccine-like function and inhibited the activity of immune-suppressive Tregs with the help of α-PD-1; thus, the distant tumor cells were attacked (Fig. 8e). Moreover, in the distant tumor tissues of the mice in the FZGM + laser + mag group, the expression of CD86 was the highest and that of CD206 was the lowest, illustrating that TAMs mainly contain antitumoral M1-type (Fig. 8c and d).

Only with the help of FZGM, the immune checkpoint blockade can display its biggest antitumor function effect, which can also be verified from the lowest expression level of TGF-β and IL-10 in the FZGM-α-PD-1 + laser + mag group (Fig. 8i and j). Due to the down-regulation of the anti-inflammatory factors, the inflammatory reaction was caused and the expression of the tumor killer cytokines such as TNF-α, IFN-γ, and IL-12 was up-regulated in group IV (Fig. 8f–h). It is worth noting that the changes in the secretion level of granzyme B in the four groups are obvious and their secretions in group IV are much higher than that in the other three groups, which

also indicate that the ability of killing the metastatic tumor cells is the best when FZGM is used in combination with the α-PD-1 antibody.[44]

To further confirm the immune response triggered by the FZGM hybrid nanozyme and the α-PD-1 antibody, a simulated metastatic tumor (distant tumor) was isolated and detected by flow cytometry. It is widely known that $CD4^+$ and $CD8^+$ T cells are two main subgroups of T cells; the population of $CD4^+$ and $CD8^+$ T cells increased obviously in group IV (Fig. 9a). In addition, the repolarization from the M2 to M1 macrophages induced by FZGM was also verified through flow cytometric analysis in Fig. 9b. The ratio of the M1 macrophages in group IV reached 31.6% and the CD86 positive ratio in the FZGM + laser + mag group (22.7%) was higher than that in the PBS group (6.67%), implying that FZGM can induce macrophage repolarization under laser irradiation. The remission of immunosuppression could also be investigated and the result is given in Fig. 9c. The $CD4^+$ T cells can be divided into two types—Treg cells and effective T cells; the former suppresses tumor immunogenicity. Therefore, the significant decrease in the Treg cells in group IV demonstrated the enhanced immune function compared with the other groups.

Scheme 2 The mechanism of anti-tumor immune responses induced by the FZGM nanozyme in combination with checkpoint blockade therapy.
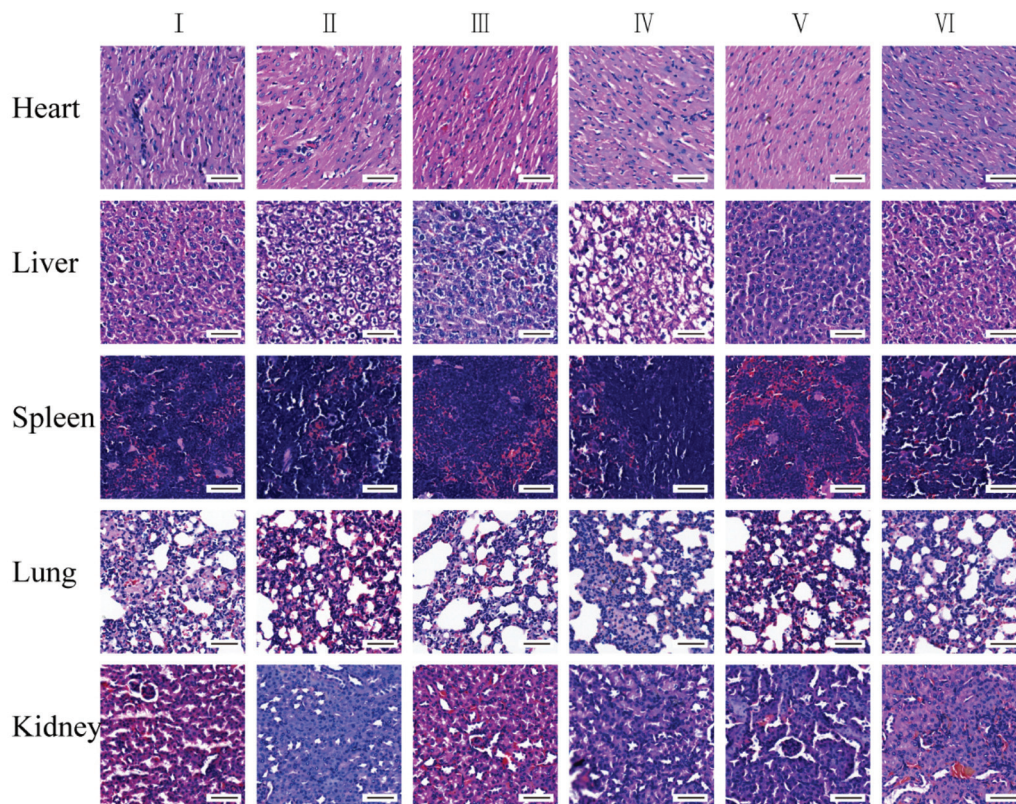
Fig. 10 H&E staining of major organs in different treatment groups (I: PBS, II: α-PD-1, III: FZGM + laser, IV: FZGM + magnetic targeting (mag), V: FZGM + laser + mag, VI: FZGM-α-PD-1 + laser + mag). Scale bar is 50 μm (808 nm laser irradiation, 1.0 W cm^{-2}).

Based on the results above, the mechanism of action of the FZGM-mediated combined therapy for primary and distant tumors was proposed (Scheme 2). Under the effect of PTT, CDT, and starvation therapy, the necrosis and apoptosis of cancer cells was triggered to generate cell debris and release the TAAs; meanwhile, the immunosuppressive TME was destructed. TAAs were captured by DCs and decomposed into antigen peptides after migration to the spleen, lymph nodes, and other immune organs. The formed MHC-peptide complex was presented to T cells and T cell-mediated specific tumor immune response was activated. At the same time, Fe$_3$O$_4$ NPs can transform the pro-tumoral M2 type macrophages to anti-tumoral M1 type and the expression of the anti-inflammatory cytokines (IL-10, TGF-β) was down-regulated, thus initiating the inflammatory reaction. Then, the immune cells and immunologic factors were recruited to produce TNF-α, IFN-γ, IL-12, and other tumor killing cytokines, which can directly induce the apoptosis of the tumor cells. In addition, α-PD-1, given in combination with the FZGM nanomedicine, can effectively reduce the inhibition signal of T cell activation and down-regulate the over-expression of Tregs. Thus, antitumor-specific immune response was enhanced and antigen-specific CD8$^+$ T lymphocytes can recognize the MHC-peptide presented by mature DCs to destroy the tumor cells by the secretion of Granzyme-B and other tumor apoptosis factors.

In addition, major organs from different groups were collected and investigated after 9 days of treatment. The H&E staining imaging of the tissues in the heart, liver, spleen, lung, and kidney show that there is no apparent histopathological change in the major organs in the control group and the treated groups (Fig. 10), which indicated that FZGM has good biosafety.

Conclusion

In summary, we designed and developed the Fe$_3$O$_4$/GOx@ZIF-8@MnO$_2$ core–shell hybrid enzyme and demonstrated its excellent performance in tumor magnetic targeting, TME response, and photothermal enhanced CDT/starvation therapy for cancer treatment. After capture by the tumor cells, MnO$_2$ and the ZIF-8 shell collapsed, and O$_2$ generated in the reaction of MnO$_2$ with H$_2$O$_2$ in TME can be used by GOx in the mesopores of ZIF-8. The gluconic acid and H$_2$O$_2$ produced in the oxidation of glucose provided conditions for the deep tumor cell penetration of Fe$_3$O$_4$, resulting in cascade amplification of the therapeutic effect. At the same time, due to the superior photothermal performance of Fe$_3$O$_4$, the reactivity of MnO$_2$, Gox, and Fe(II) could be enhanced by 808 nm laser irradiation. Under the combined action of photothermal ablation of Fe$_3$O$_4$, toxic ˙OH, and immune checkpoint blockade,

not only was the primary tumor killed but distant metastasis was also inhibited. In general, the design of the hybrid nanozyme nanoplatform provides ideas for the application of nanozymes in tumor therapy by TME modulation and tumor therapy.

Experimental

Materials and reagents

All the reagents were of analytical grade and used without any purification. Ferric chloride hexahydrate ($FeCl_3 \cdot 6H_2O$), sodium acetate (NaAc), trisodium citrate dehydrate ($C_6H_5Na_3O_7$), potassium permanganate ($KMnO_4$), ethylene glycol, and methanol were obtained from Sinopharm Group Co., Ltd (Shanghai, China). Zinc nitrate hexahydrate (Zn $(NO_3)_2 \cdot 6H_2O$) and glucose oxidase (GOx) were purchased from Aladdin Chemistry Co., Ltd (Shanghai, China). 2-Methylimidazole (2-MeIm) was received from Shanghai Macklin Biochemical Co., Ltd (Shanghai, China). Roswell Park Memorial (RPMI) 1640 medium, Penicillin–Streptomycin Liquid, and Cell Counting Kit-8 (CCK-8) were purchased from Beijing Solarbio Science & Technology Co., Ltd. Fetal bovine serum (FBS) was obtained from Procell Life Science & Technology Co., Ltd. 5-Aminofluorescein (5-AF) was obtained from Macklin Co., Ltd.

Synthesis of Fe_3O_4

Fe_3O_4 NPs were prepared by a solvothermal method: 1.14 g $FeCl_3 \cdot 6H_2O$ and 2.4 g NaAc with 0.65 g $C_6H_5Na_3O_7$ were dissolved in 50 mL ethylene glycol and magnetically stirred for 30 min at the room temperature. Then, the solution was transferred to a Teflon-sealed autoclave and heated at 200 °C for 10 h. The Fe_3O_4 NPs were separated and washed with deionized water and methanol. Finally, the NPs were dried under vacuum at the ambient temperature.

Synthesis of Fe_3O_4@ZIF-8 sample

In a typical procedure, Fe_3O_4 NPs dispersion liquid (4 mL, 0.25 mg mL^{-1}) was added to 2-MeIm in methanol solution (26 mL, 0.82 g). The mixture was treated with ultrasound for 30 min, and 10 mL of Zn $(NO_3)_2 \cdot 6H_2O$ in methanol (30 mmol L^{-1}) was added and kept at the room temperature for 1 h. Finally, the product was separated and washed with methanol.

Synthesis of Fe_3O_4@ZIF-8/GOx

20 mg Fe_3O_4@ZIF-8 was dispersed into 10 mL deionized water. Then, GOx was added into the solution. After stirring for 24 h, the products were collected by centrifugation at 8000 rpm for 10 min, followed by washing three times using deionized water and drying in a vacuum freeze-drying oven for 24 h.

Synthesis of Fe_3O_4@ZIF-8/GOx@MnO_2

$KMnO_4$ aqueous solution (10 mL, 10 mg mL^{-1}) was added into Fe_3O_4@ZIF-8/GOx aqueous solution (5 mL, 10 mg mL^{-1}) drop by drop. After sonication for 3 h, FZGM was obtained by cen-trifugation (4000 rpm, 10 min). Finally, the product was separated using a magnet and washed 3 times with deionized water.

Cell culture

4T1 cells were purchased from Procell Life Scientific & Technology Co., Ltd, China. The cells were cultured in RPMI 1640 medium supplemented with 10% fetal bovine serum and 1% penicillin–streptomycin liquid in 5% CO_2 at 37 °C in the cell incubator.

Live-dead cell staining

Calcein acetoxymethyl ester (AM, green) and propidium iodide (PI, red) staining reagents were used to stain the live and dead cells, respectively. Typically, 4T1 cells were incubated with RPMI 1640 medium at 37 °C in 5% CO_2 overnight and then the medium was replaced with a fresh one containing Fe_3O_4, FZG, FZGM, and FZGM. After treating for 10 h, the laser groups were exposed to 808 nm laser at a power density of 1 W cm^{-2} for 5 min. Cells in the control group were only treated with PBS. Subsequently, the cultured cells were stained with Calcien AM and PI solution for 30 min, and the fluorescent images of AM (λ_{ex} = 488 nm, λ_{em} = 515 nm) and PI (λ_{ex} = 488/ 545 nm, λ_{em} = 617 nm) were detected by CLSM.

Antitumor efficacy in vivo

Female Kunming mice (6 weeks old) were acquired for the in vivo anti-tumor experiments. All animal procedures were performed in accordance with the Guidelines for Care and Use of Laboratory Animals of Qingdao Agricultural University and experiments were approved by the Ethics Committee of Qingdao Agricultural University. The 4T1 tumor model was established by subcutaneous injection with 4T1 cells (1 × 10^6) into the right armpit of each healthy Kunming mice into six groups. Among them, the mice in groups I, II, V, and VI were also injected with the 4T1 cells into the left axilla to obtain double tumor animal models. In vivo therapy was given until the tumor size reached an approximate volume of 200 mm^3. 4T1 tumor-bearing mice were stochastically allocated into six groups: I: PBS, II: α-PD-1, III: FZGM + laser, IV: FZGM + mag, V: FZGM + laser + mag, VI: FZGM-α-PD-1 + laser + mag. The FZGM solution (3.0 mg kg^{-1}) was injected into the tail vein and then a magnet with a radius of 0.3 cm (magnetic field strength = 0.2 T) was fixed to the right tumor region so as to mediate the accumulation of FZGM in the tumor site for 2 h. At 2 h after tail vein injection, the right tumor site was exposed to an 808 nm laser at a power density of 1 W cm^{-2} for 5 min. Subsequently, the mice in groups I, II, V, and VI were intravenously injected with 500 µg kg^{-1} of α-PD-1 per mouse on days 3, 5, and 7. The mice were weighted every day, sacrificed every two days to collect the tumor tissues, and the volumes were recorded during treatment. Furthermore, the relative tumor volume V/V_0 (V_0 was the mean of the original volume of the tumor on the first day) was calculated according to the formula: V_{tumor} = (width^2 × length)/2.

Conflicts of interest

There are no conflicts to declare.

Acknowledgements

References

1 X. Nie, L. Xia, H. Wang, G. Chen, B. Wu, T. Zeng, C. Hong, L. Wang and Y. You, Photothermal therapy nanomaterials boosting transformation of Fe(III) into Fe(II) in tumor cells for highly improving chemodynamic therapy, *ACS Appl. Mater. Interfaces*, 2019, **11**, 31735–31743.

2 X. Liu, B. Yan, Y. Li, X. Ma, W. Jiao, K. Shi, T. Zhang, S. Chen, Y. He, X. Liang and H. Fan, Graphene oxide-grafted magnetic nanorings mediated magnetothermodynamic therapy favoring reactive oxygen species-related immune response for enhanced antitumor efficacy, *ACS Nano*, 2020, **14**, 1936–1950.

3 J. Q. Yan, J. Chen, N. Zhang, Y. D. Yang, W. W. Zhu, L. Li and B. He, Mitochondria-targeted tetrahedral DNA nanostructures for doxorubicin delivery and enhancement of apoptosis, *J. Mater. Chem. B*, 2020, **8**, 492–503.

4 X. W. Wang, X. Y. Wang, Q. F. Yue, H. Z. Xu, X. Y. Zhong, L. Sun, G. Q. Li, Y. h. Gong, N. Y. Yang, Z. Wang and Z. Liu, Liquid exfoliation of TiN nanodots as novel sonosensitizers for photothermal-enhanced sonodynamic therapy against cancer, *Nano Today*, 2021, **39**, 101170.

5 X. W. Wang, X. Y. Zhong and L. Cheng, Titanium-based nanomaterials for cancer theranostics, *Coord. Chem. Rev.*, 2020, 213662.

6 M. Chang, M. Wang, M. Wang, M. Shu, B. Ding, C. Li, M. Pang, S. Cui, Z. Hou and J. Lin, A multifunctional cascade bioreactor based on hollowstructured Cu_2MoS_4 for synergetic cancer chemo-dynamic therapy/starvation therapy/phototherapy/immunotherapy with remarkably enhanced efficacy, *Adv. Mater.*, 2019, **31**, 1905271.

7 C. Hu, L. Cai, S. Liu, Y. Liu, Y. Zhou and M. Pang, Copper-doped nanoscale covalent organic polymer for augmented photo-/chemodynamic synergistic therapy and immunotherapy, *Bioconjugate Chem.*, 2020, **31**, 1661–1669.

8 J. Q. Yan, N. Zhang, Z. Z. Zhang, W. W. Zhu, B. Li, L. Li, Y. J. Pu and B. He, Redox-responsive polyethyleneimine/tetrahedron DNA/doxorubicin nanocomplexes for deep cell/tissue penetration to overcome multidrug resistance, *J. Controlled Release*, 2021, **329**, 36–49.

9 X. W. Wang, X. Y. Zhong, L. X. Bai, J. Xu, F. Gong, Z. L. Dong, Z. J. Yang, Z. J. Zeng, Z. Liu and L. Cheng, Ultrafine Titanium Monoxide (TiO_{1+x}) Nanorods for Enhanced Sonodynamic Therapy, *J. Am. Chem. Soc.*, 2020, **142**, 6527–6537.

10 X. W. Wang, X. Y. Wang, X. Y. Zhong, L. Sun, G. Q. Li, Z. J. Yang, Y. H. Gong, Z. Liu and L. Cheng, $V-TiO_2$ nanospindles with regulating tumor microenvironment performance for enhanced sonodynamic cancer therapy, *Appl. Phys. Rev.*, 2020, **7**, 041411.

11 S. J. Peng, B. Ouyang, Y. Men, Y. Du, Y. Cao, R. Xie, Z. Pang, S. Shen and W. L. Yang, Biodegradable zwitterionic polymer membrane coating endowing nanoparticles with ultra-long circulation and enhanced tumor photothermal therapy, *Biomaterials*, 2019, **231**, 119680.

12 Z. Zhao, W. Q. Wang, C. X. Li, Y. Q. Zhang, T. R. Yu, R. F. Wu, J. Y. Zhao, Z. Liu, J. Liu and H. J. Yu, Reactive oxygen species–activatable liposomes regulating hypoxic tumor microenvironment for synergistic photo/chemodynamic therapies, *Adv. Funct. Mater.*, 2019, **29**, 1905013.

13 Z. M. Tang, H. Zhang, Y. Liu, D. Ni, H. Zhang, J. Zhang, Z. Yao, M. He, J. Shi and W. Bu, Antiferromagnetic pyrite as the tumor microenvironment-mediated nanoplatform for self-enhanced tumor imaging and therapy, *Adv. Mater.*, 2017, 1701683.

14 S. Wang, L. Yang, H. Cho, S. D. Chueng, Z. Hepeng, Q. Zhang and K. Lee, Programmed degradation of a hierarchical nanoparticle with redox and light responsivity for self-activated photo-chemical enhanced chemodynamic therapy, *Biomaterials*, 2019, **224**, 119498.

15 Q. Zhang, Q. Guo, Q. Chen, X. Zhao, S. J. Pennycook and H. Chen, Highly efficient 2D NIR-II photothermal agent with fenton catalytic activity for cancer synergistic photothermal–chemodynamic therapy, *Adv. Sci.*, 2019, **10**, 201902576.

16 R. Deng, M. Zou, D. Zheng, S. Peng, W. Liu, X. Bai, A. Chen, Y. Sun, P. Zhou and X. Zhang, Nanoparticles from cuttlefish ink inhibit tumor growth by synergizing immunotherapy and photothermal therapy, *ACS Nano*, 2019, **13**, 8618–8629.

17 L. Wang, M. Wang, B. Zhou, F. Zhou, C. Murray, R. A. Towner, N. Smith, D. Saunders, G. Xiea and W. R. Chen, PEGylated reduced-graphene oxide hybridized with Fe_3O_4 nanoparticles for cancer photothermal-immunotherapy, *J. Mater. Chem. B*, 2019, **7**, 7406–7420.

18 Q. Chen, L. Xu, C. Liang, C. Wang, R. Peng and Z. Liu, Photothermal therapy with immune-adjuvant nanoparticles together with checkpoint blockade for effective cancer immunotherapy, *Nat. Commun.*, 2016, **7**, 13193–13205.

19 J. Wang, Y. Chang, H. Luo, W. Jiang, L. Xu, T. Chen and X. Zhu, Designing immunogenic nanotherapeutics for photothermal-triggered immunotherapy involving reprogramming immunosuppression and activating systemic antitumor responses, *Biomaterials*, 2020, **255**, 120153.

20 H. J. Zhao, B. Zhao, L. Wu, H. Xiao, K. Ding, C. Zheng, Q. Song, L. Sun, L. Wang and Z. Zhan, Amplified cancer immunotherapy of a surface-engineered antigenic microparticle vaccine by synergistically modulating tumor microenvironment, *ACS Nano*, 2019, **13**, 12553–12566.

21 Q. Fu, Z. Li, J. Ye, Z. Li, F. Fu, S. Lin, C. A. Chang, H. Yang and J. Song, Magnetic targeted near-infrared II PA/MR imaging guided photothermal therapy to trigger cancer immunotherapy, *Theranostics*, 2020, **10**, 4997–5020.

22 B. Zhou, Q. Wu, M. Wang, A. Hoover, X. Wang, F. Zhou, R. A. Towner, N. Smith, D. Saunders, J. Song, J. Qu and W. R. Chen, Immunologically modified $MnFe_2O_4$ nanoparticles to synergize photothermal therapy and immunotherapy for cancer treatment, *Chem. Eng. J.*, 2020, **396**, 125239.

23 Y. Liu, J. Wu, Y. Jin, W. Zhen, Y. Wang, J. Liu, L. Jin, S. Zhang, Y. Zhao, S. Song, Y. Yang and H. Zhang, Copper(I) phosphide nanocrystals for in situ self-generation magnetic resonance imaging-guided photothermal enhanced chemodynamic synergetic therapy resisting deep-seated tumor, *Adv. Funct. Mater.*, 2019, **29**, 1904678.

24 S. Fu, R. Yang, L. Zhang, W. Liu, G. Du, Y. Cao, Z. Xu, H. Cui, Y. Kang and P. Xue, Biomimetic CoO@AuPt nanozyme responsive to multiple tumor microenvironmental clues for augmenting chemodynamic therapy, *Biomaterials*, 2020, **257**, 120279.

25 M. Zhang, W. Wang, F. Wu, T. Zheng, J. Ashleya, M. Mohammadniaeia, Q. Zhang, Q. Wang, L. Lie, J. Shen and Y. Sun, Biodegradable poly(γ-glutamic acid)@glucose oxidase@carbon dot nanoparticles for simultaneous multimodal imaging and synergetic cancer therapy, *Biomaterials*, 2020, **252**, 120106.

26 Z. Lu, J. Gao, C. Fang, Y. Zhou, X. Li and G. Han, Porous Pt nanospheres incorporated with GOx to enable synergistic oxygen-inductive starvation/electrodynamic tumor therapy, *Adv. Sci.*, 2020, **9**, 2001223.

27 Q. Cheng, F. Gao, W. Yu, M. Zou, X. Ding, M. Li, S. Cheng and X. Zhang, Near-infrared triggered cascade of antitumor immune responses based on the integrated core–shell nanoparticle, *Adv. Funct. Mater.*, 2020, **2000335**, 12.

28 L. Ding, X. Lin, Z. Lin, Y. Wu, X. Liu, J. Liu, M. Wu, X. Zhang and Y. Zeng, Cancer cell-targeted photosensitizer and therapeutic protein co-delivery nanoplatform based on a metal-organic framework for enhanced synergistic photodynamic and protein therapy, *ACS Appl. Mater. Interfaces*, 2020, **12**, 36906–36916.

29 H. Wang, Y. Chen, J. Shang, H. Wang, M. Pan, X. Liu, X. Zhou and F. Wang, Multifunctional hypoxia-involved gene silencing nanoplatform for sensitizing photochemotherapy, *ACS Appl. Mater. Interfaces*, 2020, **12**, 34588–34598.

30 Q. Jiang, K. Wang, X. Zhang, B. Ouyang, H. Liu, Z. Pang and W. Yang, Platelet membrane-camouflaged magnetic nanoparticles for ferroptosis-enhanced cancer immunotherapy, *Small*, 2020, **17**, 2001704.

31 Y. Pan, Y. Liu, G. Zeng, L. Zhao and Z. Lai, Rapid synthesis of zeolitic imidazolate framework-8 (ZIF-8) nanocrystals in an aqueous system, *Chem. Commun.*, 2011, **47**, 2071–2073.

32 M. Zhu, J. B. Jasinski and M. A. Carreon, Growth of zeolitic imidazolate framework-8 crystals from the solid–liquid interface, *J. Mater. Chem.*, 2012, **22**, 7684–7686.

33 X. Du, T. Z. Liu, F. F. Xue, X. J. Cai, Q. Chen, Y. Y. Zheng and H. R. Chen, Fe_3O_4 mesocrystals with distinctive magnetothermal and nanoenzyme activity enabling self-reinforcing synergistic cancer therapy, *ACS Appl. Mater. Interfaces*, 2020, **12**, 19285–19294.

34 Y. H. Zhong, L. Yu, Z. F. Chen, H. P. He, F. Ye, G. Cheng and Q. X. Zhang, Microwave-assisted synthesis of Fe_3O_4 nanocrystals with predominantly exposed facets and their heterogeneous UVA/fenton catalytic activity, *ACS Appl. Mater. Interfaces*, 2017, **9**, 29203–29212.

35 D. J. Ma, Q. L. Zhu, X. T. Li, H. C. Gao, X. F. Wang, X. W. Kang and Y. Tian, Unraveling the impact of ether and carbonate electrolytes on the solid-electrolyte interface and the electrochemical performances of ZnSe@C corelshell composites as anodes of Lithium-ion batteries, *ACS Appl. Mater. Interfaces*, 2019, **11**, 8009–8017.

36 J. Xu, W. Han, P. Yang, T. Jia, S. Dong, H. Bi, A. Gulzar, F. He, J. Lin and C. Li, Tumor microenvironment-responsive mesoporous MnO_2-coated upconversion nanoplatform for self-enhanced tumor theranostics, *Adv. Funct. Mater.*, 2018, **28**, 1803804.

37 Q. Wang, Y. S. Ji, J. S. Shi and L. L. Wang, NIR-driven water splitting H_2 production nanoplatform for H_2mediated cascade-amplifying synergetic cancer therapy, *ACS Appl. Mater. Interfaces*, 2020, **12**, 23677–23688.

38 Z. Wang, B. Liu, Q. Sun, S. Dong, Y. Kuang, Y. Dong, F. He, S. Gai and P. Yang, Fusiform-like Copper(II)-based metal-organic framework through relief hypoxia and GSH-depletion co-enhanced starvation and chemodynamic synergetic cancer therapy, *ACS Appl. Mater. Interfaces*, 2020, **12**, 17254–17268.

39 S. P. Chen, Q.,N. Wu, M. Wen, Q. S. Wu, J. Q. Li, Y. Cui, N. Pinna, Y. F. Fan and T. Wu, Sea-sponge-like structure of nano-Fe_3O_4 on skeletonC with long cycle life under high rate for Li-Ion batteries, *ACS Appl. Mater. Interfaces*, 2018, **10**, 19656–19663.

40 C. Li, Y. Zhang, X. Dong, L. Zhang, X. Liu, B. Li, M. Zhang, J. Feng and X. Zhang, Artificially reprogrammed macrophages as tumor-tropic immunosuppression-resistant biologics to realize therapeutics production and immune activation, *Adv. Mater.*, 2018, **31**, 1807211.

41 Q. Y. Jia, J. C. Ge, W. M. Liu, X. L. Zheng, S. Q. Chen, Y. M. Wen, H. Y. Zhang and P. F. Wang, A magnetofluorescent carbon dot assembly as an acidic H_2O_2-driven oxygenerator to regulate tumor hypoxia for simultaneous bimodal imaging and enhanced photodynamic therapy, *Adv. Mater.*, 2018, 1706090.

42 L. Luo, M. Z. Iqbal, C. Liu, J. Xing, O. U. Akakuru, Q. Fang, Z. Li, Y. Dai, A. Li, Y. Guan and A. Wu, Engineered nano-immunopotentiators efficiently promote cancer immunotherapy for inhibiting and preventing lung metastasis of melanoma, *Biomaterials*, 2019, **223**, 119464.

43 G. Yu, L. Rao, H. Wu, L. Yang, L. Bu, W. Deng, L. Wu, X. Nan, W. Zhang, X. Zhao, W. Liu and Z. Sun, Myeloid-derived suppressor cell membrane-coated magnetic nanoparticles for cancer theranostics by inducing macrophage

polarization and synergizing immunogenic cell death, *Adv. Funct. Mater.*, 2018, **28**, 1801389.

44 X. Liu, J. Zheng, W. Zhao, Y. Li, N. Gong, Y. Wang, X. Ma, T. Zhang, L. Zhao, Y. Hou, J. Wu, Y. Du, H. Fan, J. Tian and X. Liang, Ferrimagnetic vortex nanoring-mediated mild magnetic hyperthermia imparts potent immunological effect for treating cancer metastasis, *ACS Nano*, 2019, **13**, 8811–8825.